# Complex dielectric function of GaAs$_{1-x}$Bi$_x$ as a function of Bi content

Mahsa Mahtab,[1,*] Ron Synowicki,[2] Vahid Bahrami-Yekta,[1] Lars C. Bannow,[3]
Stephan W. Koch,[3] Ryan B. Lewis,[4] and Thomas Tiedje[1]

[1]*Department of Electrical and Computer Engineering, University of Victoria, Victoria, British Columbia, Canada V8W 2Y2*
[2]*J. A. Woollam Co., Inc., 645 M Street, Suite 102, Lincoln, Nebraska 68508, USA*
[3]*Department of Physics and Materials Science Center, Philipps-Universität Marburg, 35032 Marburg, Germany*
[4]*Paul-Drude-Institut für Festkörperelektronik, Hausvogteiplatz 5-7, Berlin 10117, Germany*

The complex dielectric constants of GaAs$_{1-x}$Bi$_x$ alloys grown by molecular beam epitaxy with $x = 0\%$ to 17% have been measured over the spectral range from 0.37 to 9.1 eV using spectroscopic ellipsometry. Critical points in the joint density of states have been analyzed by fitting the line shape of the Van Hove singularities in the dielectric function derived from the ellipsometry data. The critical points generally match similar critical points in the dielectric function of GaAs with at least one alternative critical point. The energy of the critical points involving transitions from the top of the valence band show a strong dependence on Bi concentration similar to the composition dependence of the band gap, while the other critical points have a weaker dependence on Bi concentration. The measured composition dependence of the band gap and the energy of the split-off hole band are in good agreement with density functional calculations. The composition dependence of the index of refraction in the vicinity of the band gap for GaAs$_{1-x}$Bi$_x$ alloys is an order of magnitude larger than the composition dependence of the index of refraction in Ga$_{1-x}$In$_x$As alloys.

## I. INTRODUCTION

Bismuth containing III–V semiconductor alloys are promising materials for applications in long-wavelength optoelectronic devices [1]. In GaAs$_{1-x}$Bi$_x$ alloys, there is a giant band-gap bowing effect with Bi alloying in which the band gap is reduced by 88 meV/% Bi at low Bi concentrations [2,3]. A similar giant band-gap bowing effect is observed in the dilute nitride alloys GaN$_x$As$_{1-x}$ [4] and GaN$_x$P$_{1-x}$ [5] except that the N alloying affects the bottom of the conduction band whereas Bi alloying affects the top of the valence band [6]. The strong effect of Bi alloying on the band gap enables long-wavelength materials to be grown on GaAs or Ge substrates with a comparatively small lattice mismatch [7,8]. One advantage of the large band-gap reduction with relatively modest lattice mismatch relative to GaAs is that it is possible to combine long-wavelength photonic devices ($>1\,\mu$m) with the high-reflectivity GaAs/AlAs multilayer Bragg reflectors in applications such as the vertical cavity laser [9,10].

In addition to long-wavelength device applications, GaAsBi alloys are interesting as an example of a highly mismatched semiconductor alloy. Although Bi is isoelectronic with As, the energy of the Bi valence orbitals is quite different from As, and the Bi atomic orbitals have a resonant interaction with the top of the GaAs valence band. A consequence of the large difference in the Bi and As orbital energies is that next-nearest-neighbor clusters of Bi produce shallow localized states in the band gap [11]. This phenomenon leads to anomalous optical properties including the giant band-gap bowing effect and broad photoluminescence emission spectra

[12]. The optical properties of GaAs$_{1-x}$Bi$_x$ are of fundamental importance in designing devices from this alloy system. The complex dielectric function of GaAs$_{1-x}$Bi$_x$ as a function of photon energy can in principle provide alternative insights into the electronic structure but has not been explored in detail. At photon energies below the band gap, the absorption coefficient and index of refraction can be measured by transmission measurements while above the band gap, where the penetration depth is less than 1 μm, reflection methods must be used [13].

In this paper we describe spectroscopic ellipsometry measurements [14–18] of the complex dielectric function of GaAs$_{1-x}$Bi$_x$ alloys as a function of photon energy for a wide range of Bi concentrations. Three earlier ellipsometric studies of the dielectric function of GaAsBi alloys have been reported. Ben Sedrine *et al.* [19] investigated the effect of Bi on the dielectric function for a set of GaAs$_{1-x}$Bi$_x$ layers grown by metal organic vapor phase epitaxy with five different Bi concentrations up to 3.7% over the spectral range of 1.4–5.4 eV. Tumėnas *et al.* [20] investigated molecular beam epitaxy (MBE) grown layers of GaAs$_{1-x}$Bi$_x$ with Bi contents of 3.5%, 5.2%, and 7.5% with a particular focus on the energy range 0.2–2.0 eV in the vicinity of the band gap. Bushell *et al.* [21] have reported measurements of the complex dielectric function of GaAs$_{1-x}$Bi$_x$ samples with Bi concentrations from 1% to 4.9% over the photon energy range from 1.08 to 4.96 eV.

In the present experiments we have measured the dielectric function of GaAs$_{1-x}$Bi$_x$ alloys over a wider range of Bi contents (up to 17%) and a wider energy range (0.37–8.9 eV) than the previous work. GaAs$_{1-x}$Bi$_x$ samples were grown by molecular beam epitaxy on GaAs substrates with 11 different Bi concentrations, from 1% to 17%. Eleven different

*Corresponding author: mahtab@uvic.ca

critical points have been identified and associated with optical transitions at high-symmetry points in the Brillouin zone by fitting the second derivative of the imaginary part of the dielectric function as a function of photon energy to Van Hove singularities [22]. The energies of the critical points are tracked as a function of Bi concentration, providing detailed information on the effect of Bi alloying on the band structure.

## II. EXPERIMENT

### A. MBE growth of GaAs$_{1-x}$Bi$_x$ samples

A set of 11 different GaAs$_{1-x}$Bi$_x$ samples with $0 < x < 17.1\%$ were grown on 350-μm-thick, single-side polished, semi-insulating GaAs (001) substrates in a VG V80H MBE reactor as described by Bahrami-Yekta *et al.* [10]. Ga-type effusion cells were used for Ga and Bi while a valved As cracker was used as the As$_2$ source. The GaAs substrates were heated to ∼600 °C to remove the surface oxide and then GaAs buffer layers were grown at a temperature of ∼550 °C to smooth the substrate before depositing the GaAs$_{1-x}$Bi$_x$ layer. The growth temperature was measured by diffuse reflectance spectroscopy [23] with ±5 °C accuracy. The GaAs$_{1-x}$Bi$_x$ epilayers were grown at low temperatures and close to the stoichiometric V/III condition in order to maximize the Bi incorporation for the high-concentration samples. The stoichiometric condition was determined by the onset of Ga droplet formation as detected by light scattering. The Bi incorporation was controlled by adjusting the substrate temperature during growth from 370 °C for 1% Bi incorporation down to 230 °C for 17.1% Bi incorporation. The GaAs$_{1-x}$Bi$_x$ samples were all pseudomorphically strained to match the in-plane lattice constant of the substrate. In order to avoid formation of misfit dislocations and to maintain coherently strained films, the thickness of the films was kept below the critical thickness for structural relaxation. For this reason the high-Bi-concentration samples, which have the largest lattice mismatch with the substrate, were thinner (34 nm for $x = 17\%$) than the lower-concentration samples (180 nm for $x = 1\%$). The as-grown high-Bi-concentration samples all had Bi droplets on the surface to varying degrees. These were removed by etching the samples in HCl for 2 min. We expect the HCl etching to also remove the surface oxide, although the oxide will grow back after prolonged air exposure.

The Bi content and thickness of the GaAs$_{1-x}$Bi$_x$ epilayers were measured by high-resolution x-ray $\theta$-2 scans on (004) planes using a Bruker D8 Discover diffractometer. Figure 1 shows x-ray diffraction spectra for five representative samples. The dashed lines in Fig. 1 are the simulated x-ray diffraction spectra using the dynamical x-ray diffraction simulation software LEPTOS; they show good agreement with the experimental data. The presence of well-defined pendelosung fringes indicates that the films have a relatively uniform composition and thickness with sharp interfaces. All of the samples in Fig. 1 show clear pendelosung fringes with the exception of the highest-Bi-concentration sample ($x = 17\%$) likely because of the relatively high density of Bi droplets on this sample, which tend to leave indents on the sample surface after they are removed by etching. We explored the effect on the LEPTOS fits of adding surface roughness as well as a two-layer model for the GaAsBi film in order to account
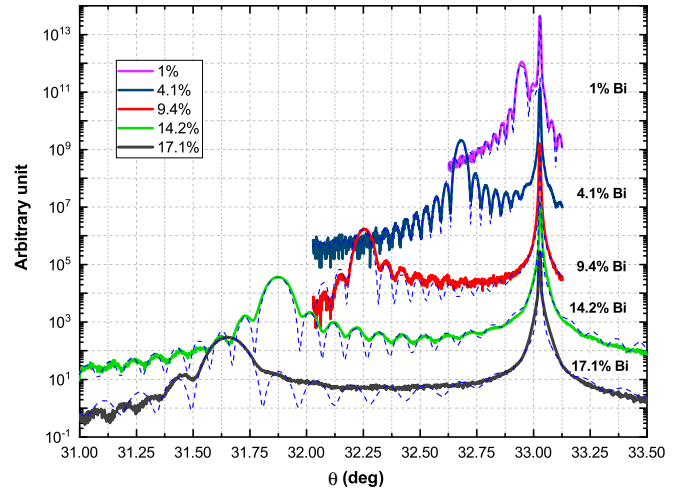


FIG. 1. High-resolution (004) x-ray diffraction data for four selected GaAs$_{1-x}$Bi$_x$ samples with indicated Bi concentrations.

for possible compositional inhomogeneity near the substrate film interface. However, we were unable to obtain a reliable estimate for the surface roughness using this approach. Figure 2 shows a comparison of the thicknesses of the 11 different samples obtained by x-ray diffraction with the thicknesses obtained from the ellipsometry measurements. The thicknesses measured by the two different methods are generally in good agreement across the entire composition range.

### B. Ellipsometry measurements

Spectroscopic ellipsometry measurements were performed with two variable angle spectroscopic ellipsometers (VASEs) made by the J. A. Woollam Co., namely, VASE and VUV-VASE, over the energy ranges 0.37–4.5 eV and 4.3–9.0 eV, respectively, with an energy spacing of 0.01 eV. The measurements were made at room temperature and at three different incidence angles, 75 °, 76 °, and 77 °. Both ellipsometers have rotating analyzers and autoretarder compensators, and in the
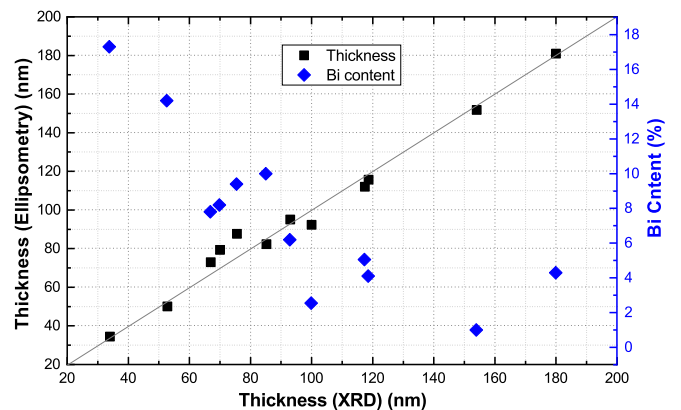


FIG. 2. Thickness of GaAs$_{1-x}$Bi$_x$ samples determined by ellipsometry compared with thickness determined by dynamical fits to x-ray diffraction data. Also shown (right scale) is the Bi content for the same samples.

case of the VUV-VASE the optical path is purged with dry nitrogen to eliminate absorption from ambient water vapor and oxygen in the vacuum UV spectral range above 6.5 eV [16,17]. The back surface of the samples was roughened to suppress unwanted back-surface reflections which occur at long wavelengths below the band gap of the substrate.

The ellipsometry method determines the real and imaginary part of the dielectric function of a sample from measurements of the polarization state of light before and after reflection from the sample. The change in the polarization of incident light upon reflection from an isotropic sample is described by two parameters $\Psi$ and $\Delta$, the so-called ellipsometric angles, which are related to the incident and reflected electromagnetic field amplitude by Eqs. (1) and (2).

$$\rho = \frac{E_{rp}E_{is}}{E_{ip}E_{rs}} = \frac{|r_p|\exp(i\delta_p)}{|r_s|\exp(i\delta_s)} = \tan\Psi\exp(i\Delta), \quad (1)$$

where

$$\tan\Psi = \frac{|r_p|}{|r_s|} \quad \text{and} \quad \Delta = \delta_p - \delta_s. \quad (2)$$

Information about the refractive index, extinction coefficient, dielectric function, and thin-film thicknesses are embedded in the Fresnel coefficients $r_p$ and $r_s$, for $p$- and $s$-polarized light, respectively, and consequently into the values of the ellipsometric angles $\Psi$ and $\Delta$ and must be extracted by fitting the $\Psi$ and $\Delta$ spectra to an accurate model of the sample structure [15–17].

For the purpose of fitting the ellipsometry data a four-layer model was used to simulate the sample. The four layers are ambient air, a surface layer which includes the effects of both surface roughness and surface oxide, the GaAs$_{1-x}$Bi$_x$ layer, and the GaAs substrate. The optical properties of the GaAs substrate are fixed and given by values from the literature [16,24]. It should be noted the GaAs substrate optical constants are published to only 6 eV, so the GaAs$_{1-x}$Bi$_x$ films are assumed fully opaque above 6 eV where reflections from the film substrate are fully absorbed before exiting the sample. This is a reasonable assumption given the large absorption values in the GaAsBi films at high energies above 4 eV make transmission through the films negligible, even for the thinnest GaAsBi film at 34 nm thickness.

GaAs-based semiconductors are known to grow a thin native surface oxide layer in ambient conditions, and ellipsometry is extremely sensitive to the presence of these thin oxide layers as discussed by Aspnes and Studna [14]. To fit the ellipsometric data it was required to include a surface layer of some type, and unfortunately, the optical constants of GaAsBi oxide are not known. The optical constants of GaAs oxide should work but are only published to 5.6 eV by Zollner [25]. Therefore, in this work the surface layer is assumed to be a mixture of surface oxide and surface roughness modeled using a Bruggeman effective medium approximation (EMA) [17,18]. In this approach the optical constants of the surface layer are modeled by a mix of the optical constants of the GaAs$_{1-x}$Bi$_x$ film below with the ambient air above with a 50% fraction of each, creating a layer with optical constant intermediate between the two. As the

optical constants of the GaAs$_{1-x}$Bi$_x$ vary, the EMA calculation automatically varies the surface layer optical constants. This surface oxide/roughness approach allows us to fit the ellipsometric data over the full measured spectral range while including the effects of the surface layer in the analysis model.

A two-step method was used to extract the optical properties of the GaAs$_{1-x}$Bi$_x$ films from the ellipsometry data. First, the thickness of the GaAs$_{1-x}$Bi$_x$ film and thickness of the surface roughness/oxide layer were determined along with the complex dielectric function of the GaAs$_{1-x}$Bi$_x$ film by fitting oscillator models to the ellipsometric data [15–18]. The thickness of the GaAs$_{1-x}$Bi$_x$ layer is determined from the long-wavelength response where the sample is weakly absorbing, while the optical constants of the GaAs$_{1-x}$Bi$_x$ layer were deduced from fitting oscillator model parameters. Both thicknesses and oscillator model parameters were adjusted together to fit the $\Psi$ and $\Delta$ spectra over the full measured spectral range from 0.37 to 9.0 eV. In the fits to $\Psi$ and $\Delta$ the optical properties of the GaAs$_{1-x}$Bi$_x$ film and the thickness and optical properties of the surface layer were treated as adjustable parameters. The analysis software automatically adjusts the thickness of the surface layer and the optical constants of the GaAs$_{1-x}$Bi$_x$ layer to obtain a best fit between the model generated data and the experimental ellipsometry data. Oscillator models gave overall good fits to the data, enforce Kramers-Kronig consistency on the optical constants [16–18], and allow determination of the thickness of the GaAs$_{1-x}$Bi$_x$ and surface layers.

However, with oscillator models there was a concern about losing small features in the dielectric function. For this reason, a second analysis step was performed by fixing the film and surface layer thicknesses at the values obtained from the oscillator model, then starting from the oscillator model results for the dielectric function and fitting the ellipsometry data at each measured wavelength for the GaAsBi film optical constants $n$ and $k$ or dielectric function $\epsilon_1$ and $\epsilon_2$. This approach increases the noise in the dielectric function data but retains fine details in the dielectric function as a function of energy.

All the data for the dielectric function presented in this paper were obtained by fitting the optical constants at each measured wavelength point after the initial oscillator model fit. See Figs. 3 and 4 for the measured real and imaginary part of the dielectric function as a function of energy for five selected Bi concentrations. The inset in Fig. 3 shows the thickness of the surface roughness layer determined from the fits to the ellipsometry data as discussed above. The trend of increasing surface roughness with increasing Bi concentration is consistent with the increase in the density and size of Bi surface droplets for high-Bi-content samples.

## III. BAND STRUCTURE

### A. Ellipsometry data analysis

Critical points (CPs) are nonsmooth points in the joint density of states (DOS) due to Van Hove singularities which occur at high-symmetry points in the Brillouin zone. CPs can be used to extract detailed information about the band structure of semiconductors. We will use the critical points to determine the effect of Bi alloying on the band structure
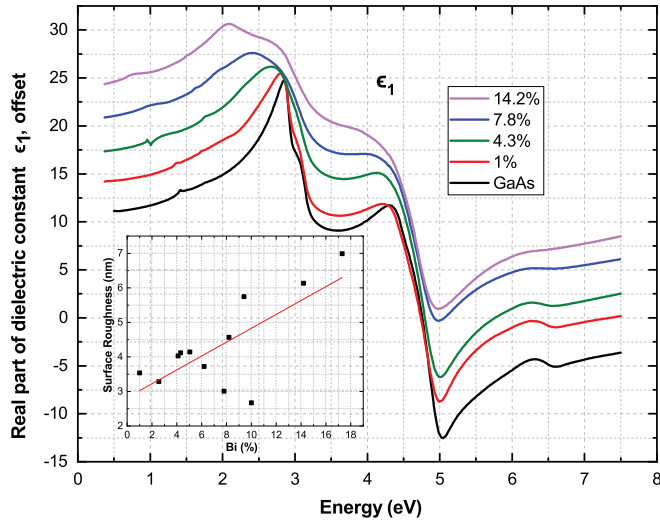
FIG. 3. Real part of the complex dielectric function $\epsilon_1$ for GaAs and four representative GaAs$_{1-x}$Bi$_x$ samples. The inset shows the thickness of the surface roughness/oxide layer as a function of Bi concentration determined from the fits to the ellipsometry data.

of GaAs$_{1-x}$Bi$_x$. As a reference, the band structure of GaAs calculated by Chelikowsky and Cohen [26], indicating the main interband critical points assigned by Lautenschlager *et al.* [22], is shown in Fig. 5. The features in the dielectric function $\epsilon(E)$ associated with critical points can be fit by standard analytic line shapes as follows [27,28].

$$\epsilon(E) = \begin{cases} \sum_{j=1}^{N} C_j - A_j e^{i\varphi_j}(E - E_{cj} + iB_j)^n & n \neq 0 \\ \sum_{j=1}^{N} C_j - A_j e^{i\varphi_j}\ln(E - E_{cj} + iB_j) & n = 0, \end{cases}$$
(3)

where the critical point parameters are the amplitude $A_j$, excitonic phase angle $\varphi_j$, energy threshold $E_{cj}$, broadening $B_j$, and critical point dimension $n$ defined by the type of extremum found in the joint DOS. The parameter $n$ equals $-1/2$ for a one-dimensional CP, $n = 0$ for a two-dimensional
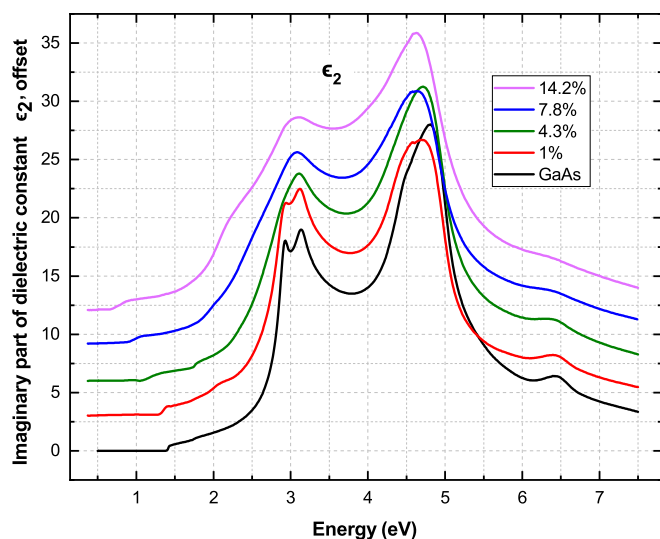


FIG. 4. Imaginary part of the dielectric function $\epsilon_2$ for GaAs and four representative GaAs$_{1-x}$Bi$_x$ samples.
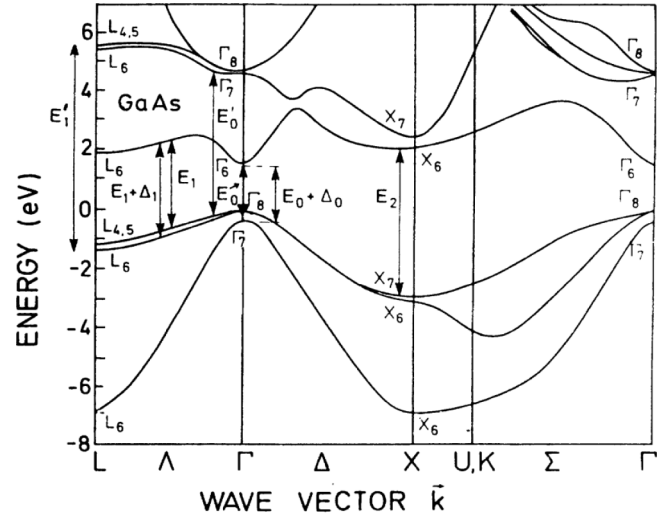


FIG. 5. Band structure of GaAs with critical points in the complex dielectric function indicated by arrows [22].

(logarithmic) CP, and $n = +1/2$ for a three-dimensional CP. In the case of a discrete exciton with a Lorentzian line shape near the band gap, $n = -1$. To make the features in the dielectric function associated with the critical points stand out against a smooth background it is convenient to take the second derivative of the experimentally measured dielectric function as a function of photon energy. The differentiation and smoothing of the dielectric function is carried out with a polynomial of degree 5 using the Savitzky-Golay method [29,30]. The critical point parameters are found by numerical fitting of the second derivative of the dielectric function with the line-shape functions in Eq. (4) below which are the second derivatives of functions in Eq. (3).

$$\frac{d^2\epsilon}{dE^2} = \begin{cases} \sum_{j=1}^{N} -n(n-1)A_j e^{i\varphi_j}(E - E_{cj} + iB_j)^{n-2} & n \neq 0 \\ \sum_{j=1}^{N} A_j e^{i\varphi_j}(E - E_{cj} + iB_j)^{-2} & n = 0 \end{cases}$$
(4)

High-quality fits to the second derivative of the imaginary part of the dielectric function can be obtained as illustrated in Fig. 6. The second derivative of the experimental dielectric function for five representative samples is shown in Fig. 6 (data points) together with the best fits to the data with the functions in Eq. (4) (solid line). The fundamental band gap $E_0$ and its spin-orbit split-off counterpart $E_0 + \Delta_0$ are the two lowest-energy critical points. These critical points have been fitted by an excitonic line shape ($n = -1$) while the other optical transitions have been fit by two-dimensional (2D) critical points ($n = 0$), following Lautenschlager *et al.* [22]. The number of critical points ($N$) in Eq. (3) is increased until the best agreement with the experimental spectrum is achieved and finally the fitting parameters are extracted.

### B. Density functional theory calculations

Density functional theory (DFT) calculations for supercells containing 128 atoms with Bi concentrations from $1.56 < x < 10.94\%$ have been performed utilizing the projector augmented-wave pseudopotential method [31,32] as
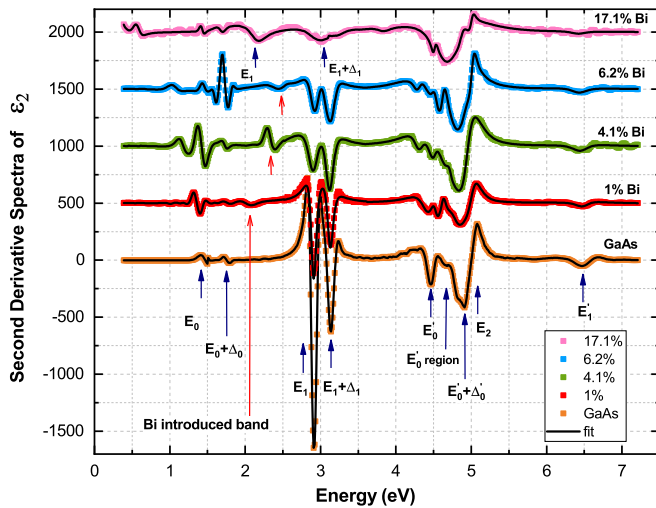
FIG. 6. Second derivative of the measured imaginary part of the dielectric constant of GaAs and four representative GaAs$_{1-x}$Bi$_x$ samples with Bi concentrations of 1%, 4.1%, 6.2%, and 17.1%. The solid lines are best fits to the data using the model described in the text.



FIG. 7. Index of refraction in the vicinity of the optical band gap for GaAs and eight GaAs$_{1-x}$Bi$_x$ samples with different Bi concentrations. The measured refractive index of a GaAs substrate (black) is plotted together with values from the literature (dashed gray) [24] which overlap almost perfectly. The low-energy peak is associated with the band gap $E_0$ and the smaller peak at higher energy is the split-off hole-band transition of $E_0 + \Delta_0$.

implemented in the VIENNA *AB INITIO* SIMULATION PACKAGE [33,34]. The supercells are constructed as special quasirandom structures [35,36] with the ALLOY-THEORETIC AUTOMATED TOOLKIT [37–39]. The atom positions in the supercells were optimized with the generalized gradient approximation as parametrized for solids by Perdew *et al.* [40], using an energy cutoff of 510 eV, converging the forces below 20 meV/Å and the energies to an accuracy of 0.001 meV. For the calculation of the band gap and spin-orbit split-off transition energy, the Tran-Blaha modified Becke-Johnson potential [41] was used, the energy cutoff was 410 eV, and the energies were converged to 0.1 meV. In all cases a $2 \times 2 \times 2$ $\Gamma$-centered $k$-point mesh was used.

For pure GaAs and identical parameters, our DFT calculations yield a lattice constant of 5.653 Å, a band gap of 1.50 eV, and a spin-orbit splitting of 0.31 eV [42], all for $T = 0$ K. This compares well to the low-temperature experimental band gap of 1.52 eV and spin-orbit splitting of 0.33 eV for GaAs [22] and the experimental room-temperature values of 1.42 and 0.34 eV. In the experiment, the GaAs$_{1-x}$Bi$_x$ samples were grown pseudomorphically on GaAs substrates, thus fixing the in-plane lattice constant of GaAs$_{1-x}$Bi$_x$ to the GaAs value. In our DFT calculations, this feature was modeled by constraining the in-plane lattice constants of the supercells to the GaAs value (5.653 Å) and optimizing the lattice constant in the growth direction to obtain an energy minimum. Moreover, band structure calculation for pure GaBi resulted in a lattice constant of 6.316 Å and a negative band gap of $-1.65$ eV. This compares well to Janotti *et al.* [6] who report a lattice constant of 6.324 Å and a band gap of $-1.45$ eV for GaBi.

The Brillouin zone of the supercell is smaller than that of the primitive cell with the consequence that the resulting band structure does not easily compare with that of the primitive cell. However, the supercell states can be projected onto the states of the primitive cell. In this procedure, often referred to as unfolding, the states are assigned with a spectral weight
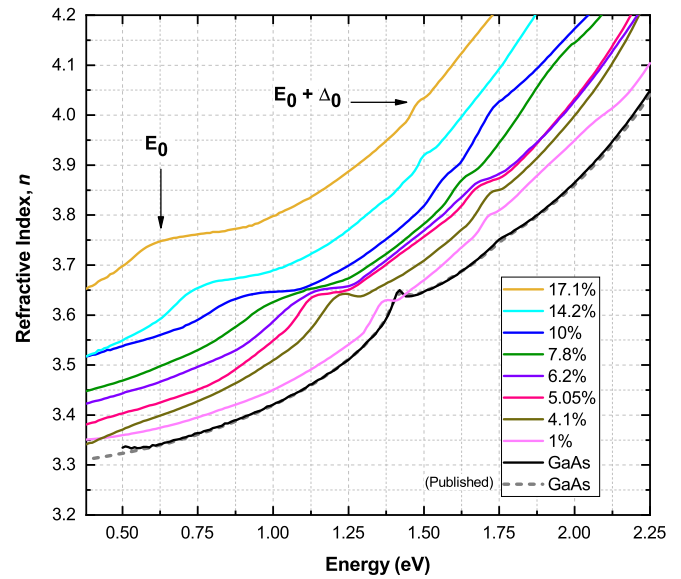
which is a measure for the amount of Bloch character of the primitive cell state contained in the unfolded supercell state and the BANDUP code has been used for the unfolding in this study [43,44].

## IV. RESULTS AND DISCUSSION

The real and imaginary parts of the dielectric constant for GaAs and four GaAs$_{1-x}$Bi$_x$ samples with representative Bi concentrations are shown in Figs. 3 and 4, respectively. The ellipsometry measurements of the optical constants of the bare GaAs substrate show excellent agreement with previously published data for GaAs [24], based on a three-layer model (air, oxide, GaAs). The intensity of the measured value for $\epsilon_2$ at 4.8 eV is considered to be a figure of merit for the quality of the sample surface and was found to be 27.97 for the GaAs substrate material. This value is higher than the highest previously recorded values for GaAs by Aspnes and Studna (25.2 and 25.59) [14].

The index of refraction and optical absorption coefficient ($\alpha = 4\pi\kappa/\lambda$) in the vicinity of the band gap are of particular interest for device applications. These quantities are plotted as a function of energy for GaAs and eight GaAs$_{1-x}$Bi$_x$ samples with varying Bi concentrations in Figs. 7 and 8, respectively.

The small features in the index of refraction of Fig. 7 are examples of critical points in the optical spectrum. The band gap shows up as a small peak in the index of refraction. For example, in the GaAs sample there is a distinct peak in the refractive index at 1.42 eV which matches the band gap. The optical band gap decreases with increasing Bi concentration as expected and the features in the index of refraction and the optical absorption associated with the band gap broaden
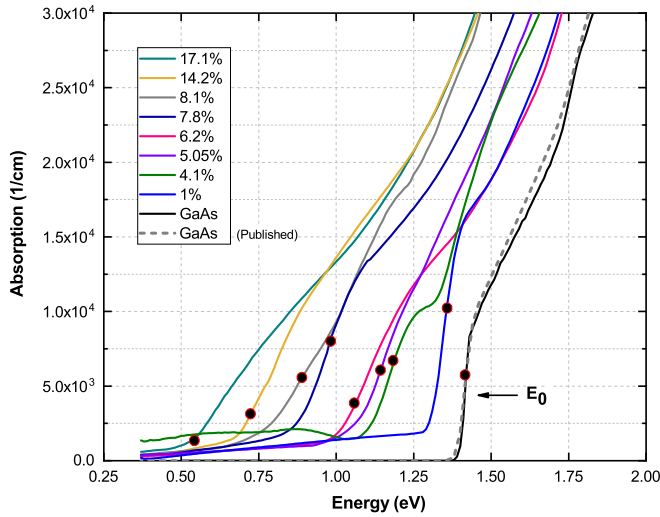
FIG. 8. Optical absorption edge for GaAs and eight GaAs$_{1-x}$Bi$_x$ samples with different compositions. The measured optical absorption of the GaAs substrate (black) is in good agreement with data from the literature (dashed gray) [24]. The solid dots are $E_0$ determined by ellipsometry.

with increasing Bi concentration. A weak feature in the index of refraction near 1.75 eV in the GaAs sample is due to the transition from the split-off hole band to the conduction band. This feature also moves to lower energy with increasing Bi concentration but not as fast as the fundamental band gap. The solid circles on the optical absorption coefficient lines in Fig. 8 indicate the band gaps calculated by ellipsometry measurement.

It is noteworthy that Bi alloying of GaAs has a much bigger effect on the refractive index than In alloying as illustrated in Fig. 9. In this figure the refractive indices of GaAs$_{1-x}$Bi$_x$ and
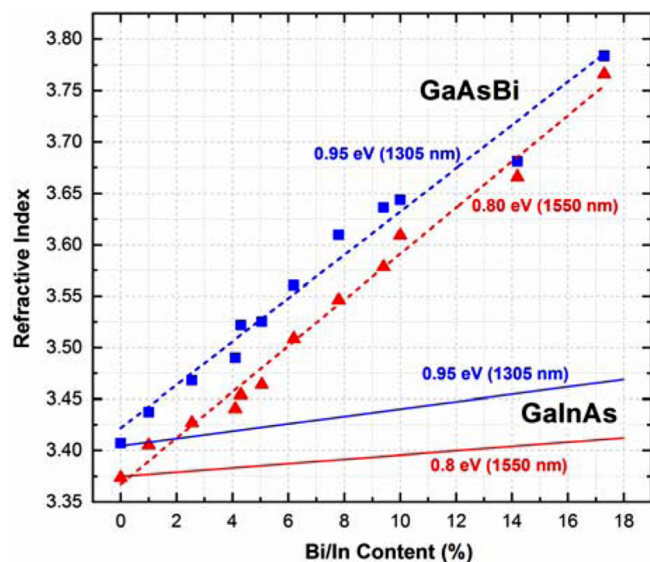


FIG. 9. Ellipsometric index of refraction at 1.3 $\mu$m (squares) and 1.55 $\mu$m (triangles) together with linear fits as a function of Bi content. Refractive indices of Ga$_{1-x}$In$_x$As for 1.3 and 1.55 $\mu$m as a function of In content are obtained from Ref. [56].
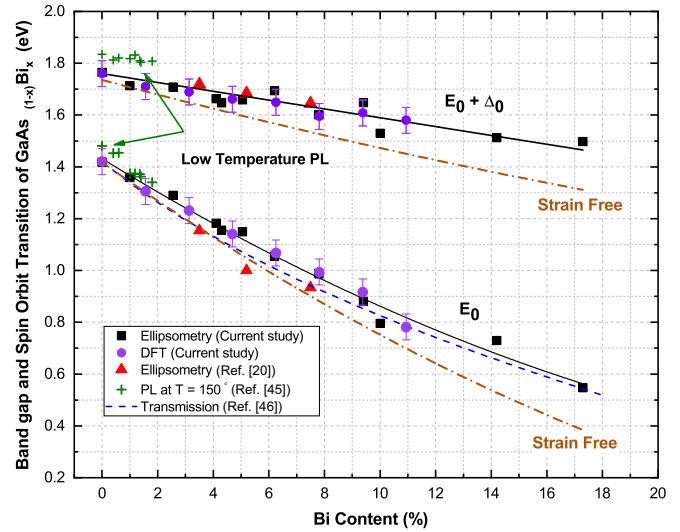


FIG. 10. The solid squares (■) are ellipsometry measurements of the optical band gap and split-off hole transition. The solid lines are fits to the ellipsometry data. The solid triangles (▲) are ellipsometry measurements by Tumėnas *et al.* [20]. The solid circles (●) are DFT calculations, with error bars giving the range of values for different arrangements of the Bi atoms in the supercell. The + symbols are low-temperature photoluminescence measurements by Fluegel *et al.* [45], the dashed line is a fit to optical transmission data from Masnadi-Shirazi *et al.* [46], and the dot-dash lines are the composition dependence of the band gap for unstrained material as discussed in the text.

Ga$_{1-x}$In$_x$As at 1.3 and 1.55 $\mu$m are plotted as a function of the concentration of the alloying elements. For the same Bi and In concentrations the refractive index change with Bi alloying is 6$\times$ greater than the change in the index with In alloying.

Figure 10 shows how the Bi concentration dependence of the band gap and split-off hole band gap obtained from our ellipsometry data and DFT calculations compare with earlier ellipsometry [20], photoluminescence [45], and optical transmission measurements [46].

We obtain the energy of the band gap and split-off hole-band transitions by fitting the ellipsometry measurements to the corresponding critical points as discussed above in the section on band structure. The DFT band gap and split-off hole-band transitions were shifted by $\Delta E_0 = -0.08$ eV and $\Delta(E_0 + \Delta_0) = -0.05$ eV, respectively, to account for the discrepancy between the DFT results and the room-temperature experimental results for GaAs as discussed above. The "error bars" in the DFT data indicate variations resulting from different supercell configurations for the same Bi concentration [42]. The agreement of the ellipsometry measurements and the DFT calculations with earlier results as well as the band anticrossing (BAC) calculation proposed by Zhao *et al.* [12] is excellent for both the fundamental band gap and the split-off hole-band transition.

The composition dependence of the band gap in III–V semiconductor alloys can be fitted with a quadratic equation [47] $E(x) = A + Bx(x-1) + Cx$ where $B$ is the bowing parameter. The best fit parameters for the composition dependence of the ellipsometric band gap in Fig. 10 are $A = $

1.42 eV, $C = 0.76$ eV, and bowing parameter of $B = 6.98$ eV. This fit is shown by the solid line in Fig. 10. Also shown in Fig. 10, by dot-dash lines, is the estimated band gap and spin-orbit split-off band gap for strain-free material. The compressive in-plane strain of the $GaAs_{1-x}Bi_x$ layers increases the band gap of the layers, which means that the unstrained material will have a lower band gap [48]. The effect of the in-plane compressive strain on the band gap in Fig. 10 is estimated from the lattice constant in the vertical direction determined experimentally by x-ray diffraction, together with the known Poisson ratio and deformation potentials for GaAs from the literature [48,49].

Zhao *et al.* [12] have analyzed the band-gap evolution of dilute $GaAs_{1-x}Bi_x$ alloys for the composition range $0 < x < 0.11$, using a band anticrossing model. Their model for the composition dependence of the band gap matches almost perfectly the composition dependence obtained by Masnadi-Shirazi *et al.* [46], shown by the dashed line in Fig. 10, which is also in good agreement with the ellipsometry data.

For the most part we are able to relate the critical points in $GaAs_{1-x}Bi_x$ to the corresponding critical points in GaAs, possibly shifted in energy. Therefore, we use the same nomenclature for the CPs of the $GaAs_{1-x}Bi_x$ alloys ($x < 0.17$) as for GaAs. As noted above, the lowest-energy CP is the fundamental band gap $E_0$ ($\Gamma_8^v \rightarrow \Gamma_6^c$) located at the $\Gamma$ point of the Brillouin zone (BZ) which involves transitions between the $\Gamma_8^v$ valence-band and $\Gamma_6^c$ conduction-band states near the origin in reciprocal space. The second-lowest-energy CP, at $E_0 + \Delta_0$, corresponds to transitions from the spin-orbit split-off hole band to the lowest conduction band ($\Gamma_7^v \rightarrow \Gamma_6^c$).

Critical points in the spectral region around 3 eV correspond to transitions at the $L$ point and along the line in $k$ space connecting the $L$ point to the $\Gamma$ point where the conduction and valence bands are nearly parallel ($\Lambda$ line). The transition from the top of the valence band to the bottom of the conduction band at the $L$ point is at energy $E_1$ ($L_6^v \rightarrow L_6^c$) and the transition from the spin-orbit split-off band to the bottom of the conduction band is at energy $E_1 + \Delta_1$ ($L_4^v \rightarrow L_6^c$). There is another critical point involving transitions at the $L$ point which is $E_1'$ of energy 6.5 eV, in which the optical transitions are from the top of the valence band to the first empty band above the conduction band. This is the highest-energy critical point that we observed. The large broadening and low signal to noise ratio may explain why the spin-orbit splitting is not observed in this critical point.

The spectral region between 4 and 5.5 eV in GaAs is complex with several overlapping critical points at different places in $k$ space. There is the $E_0'$ ($\Gamma_8^v \rightarrow \Gamma_7^c$) transition at the $\Gamma$ point with its spin-orbit split-off counterpart at $E_0' + \Delta_0'$. In addition, there are several critical points at the $X$ point in the Brillouin zone of which the transition at energy $E_2$ ($X_7^v \rightarrow X_6^c$) is the most prominent.

A total of 11 critical points were identified through fitting the second derivative line shapes for samples with Bi concentration between 1% and 8% and ten critical points were identified for the samples with higher Bi concentration. The energy of the critical points is plotted as a function of Bi concentration in Fig. 11. The width of the critical points
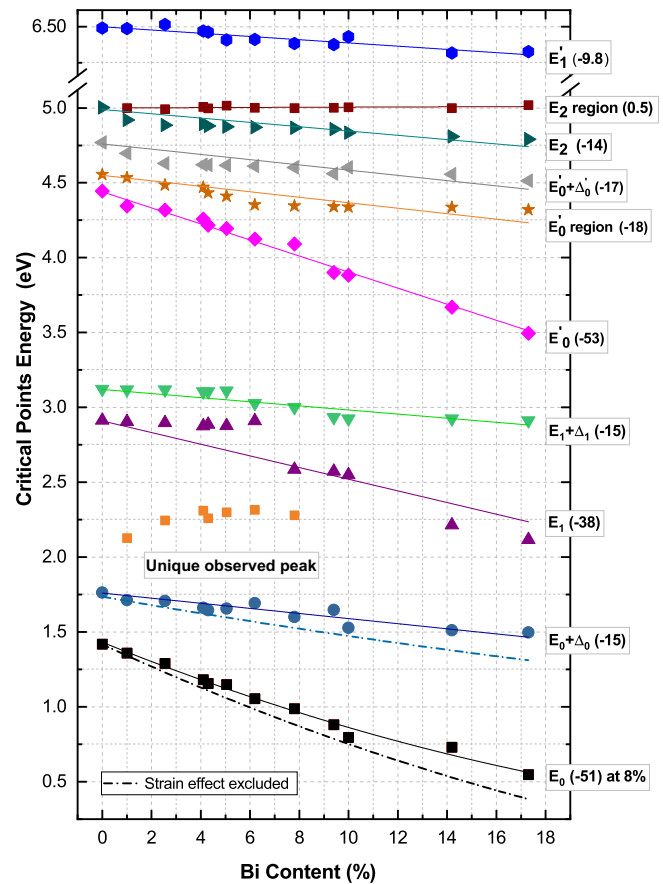


FIG. 11. Bismuth concentration dependence of the critical points in the imaginary part of the dielectric function in $GaAs_{1-x}Bi_x$. The solid lines are linear fits to the data with the exception of the fit to the band gap $E_0$ which includes a bowing parameter as discussed in the text. The numbers in brackets specify the slope of the fits in eV/%. The transition $E_0' + \Delta_0$ is forbidden by dipole selection rules [50]. The dashed line shows the effect of Bi incorporation excluding the strain effect.

increases with Bi concentration as shown in Fig. 12. The increased broadening is due to alloy fluctuations and the formation of Bi clusters on the atomic scale [5,15].

The Bi concentration dependences of the critical points are fit with straight lines in Fig. 11 except for the fundamental band gap $E_0$ which is fit with a quadratic function as discussed above. The linear fits are constrained to pass through the GaAs critical points at $x = 0$. The critical points in the 2.0–3.0 eV range labeled "unique observed peak" and $E_1$ in Fig. 11 do not show a smooth dependence on Bi concentration and the fit to the critical points labeled $E_1$ is less convincing. The slope of the best fit lines in meV/% is specified in the boxes next to the fitted lines in Fig. 11. In the case of the fundamental band gap the slope is taken at the midpoint of the fitted line. The three critical points that involve the top of the valence band, namely, $E_0$, $E_0'$ at the $\Gamma$ point and $E_1$ on the $\Lambda$ line, have a strong dependence on Bi concentration, namely, 51, 53, and 38 meV/% respectively, while the other critical points have a weaker dependence on Bi concentration (9.8–18 meV/%). The reduction in the fundamental band gap $E_0$ with increasing Bi content is primarily due to the effect of Bi alloying on
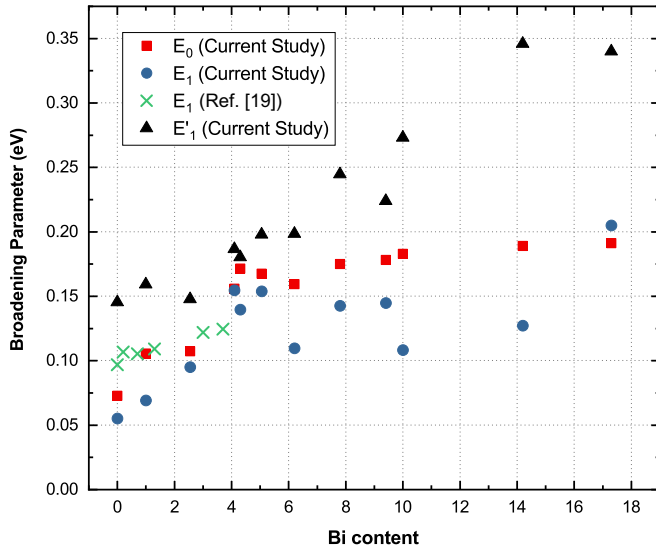
FIG. 12. Broadening parameter $B$ for three different critical points as a function of Bi concentration. Also shown is the broadening parameter measured by Ben Sedrine *et al.* [19].
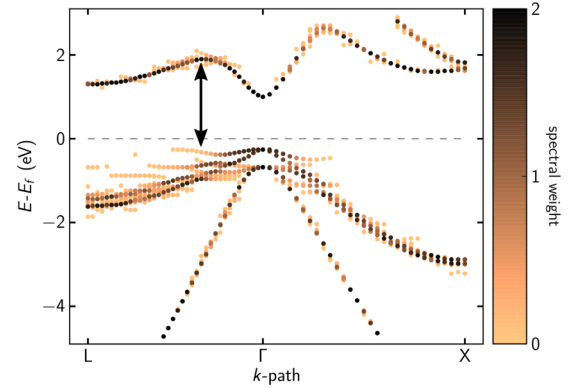


FIG. 13. Band structure for $GaAs_{1-x}Bi_x$ with $x = 1.56\%$ calculated using density functional theory and projected onto the conventional Brillouin zone for a zinc-blende crystal. The broken-up structure at the top of the valence band results from the resonant interaction of the Bi orbitals with the states forming the top of the valence band. The arrow indicates a possible critical point near 2 eV associated with Bi alloying.

the spin-orbit splitting $\Delta_0$, since the spin-orbit split-off band gap $E_0 + \Delta_0$ is by comparison relatively insensitive to Bi concentration (Fig. 11 and Ref. [45]). We assume that the Bi composition dependence of the $E_1$ transition along the $\Lambda$ line is similarly dominated by the effect of Bi alloying on the spin-orbit splitting $\Delta_1$. In this case the $\frac{2}{3}$ rule will apply ($\Delta_1 = \frac{2}{3}\Delta_0$) [50], which is consistent with the observed weaker dependence of $E_1$ on Bi concentration compared with $E_0$ in Fig. 11.

The Bi concentration dependence of the energies of the critical points discussed above confirms that the top of the valence band is the part of the band structure that is most sensitive to Bi alloying. Similar behavior is observed in the case of the dilute nitrides except that it is the bottom of the conduction band that is most sensitive to N alloying [4,5]. One of the critical points that is aligned with $E_2$ for GaAs shows no dependence on Bi concentration; it is possible that this is a residual signal from the GaAs substrate for which the $E_2$ critical point is very strong.

The 2.0–3.2 eV energy range shows three critical points at low Bi concentration, namely, $E_1$, $E_1 + \Delta_1$ plus another unidentified critical point. However, at high Bi concentration, only two critical points are observed in this energy range. The $E_1$ critical point is strong at low Bi concentration and up to $x = 6\%$ its energy is constant independent of Bi concentration. Starting at 7.8% this critical point shifts to lower energy or is replaced by another critical point at lower energy which shows a strong dependence on Bi concentration similar to the dependence of the fundamental band gap. In addition, there is a weaker unidentified CP at 2.1–2.3 eV which disappears above 7.8% or merges with the above-mentioned critical point and can no longer be distinguished as a separate CP. We propose that the complex behavior of the CPs in the 2.0–3.2 eV range is due to one or more optical transitions associated with Bi alloying. The band structure of $GaAs_{1-x}Bi_x$ can be estimated by DFT calculations of supercells as described

above. Figure 13 shows the electronic structure for a supercell with a Bi concentration of 1.56% after unfolding. As a result of the resonant interaction between the Bi orbitals and the states forming the top of the valence band, the valence-band structure is disturbed, and new bands are created, especially in the vicinity of the top of the valence band. In Fig. 13, a possible unexpected transition in the 2.0–3.2 eV energy range is indicated by an arrow, which could result in a unique critical point along the $\Lambda$ line between $\Gamma$ and $L$. This is the same energy range in which we observe the unidentified critical point and anomalous dependence of the critical point energy on Bi concentration.

The energy of the critical points measured by Ben Sedrine *et al.* [19] and Bushell *et al.* [21] in the 2.6–5.0 eV range are compared with our measurements as a function of Bi concentration in Fig. 14. In the case of the $E_1 + \Delta_1$ critical point the energies from Refs. [19,21] match almost exactly with our results. In the case of $E_1$ our results are in good agreement with Ben Sedrine *et al.* while the Bushell results for $E_1$ are somewhat lower in energy and well aligned with the linear fit to $E_1$ from Fig. 11, which is also shown in Fig. 14. The data for $E_1$ from Ref. [18] support our assignment of the fitted line to $E_1$ in Fig. 11. In the energy range 4.2–5 eV ($E_0'$, $E_0' + \Delta_0$, $E_2$) we fit our data with four critical points whereas Ben Sedrine uses two critical points; otherwise, there is general agreement on the energies. The broadening of the $E_1$ critical point as a function of Bi concentration determined by Ben Sedrine *et al.* is shown in Fig. 12. Their data show a similar increase in the width of the $E_1$ critical point with increasing Bi concentration as with our data, although Ben Sedrine's critical point is broader.

It is interesting to compare the extrapolated critical points with the band structure of GaBi. Although GaBi has not been synthesized, there are several calculated band structures [6,51–55]. The critical points in Fig. 11 that depend strongly on the Bi concentration ($E_0$, $E_1$, $E_0'$) extrapolate to negative energy at 100% Bi; similarly the strain-free version of the $E_0 + \Delta_0$ critical point also extrapolates to negative energy.
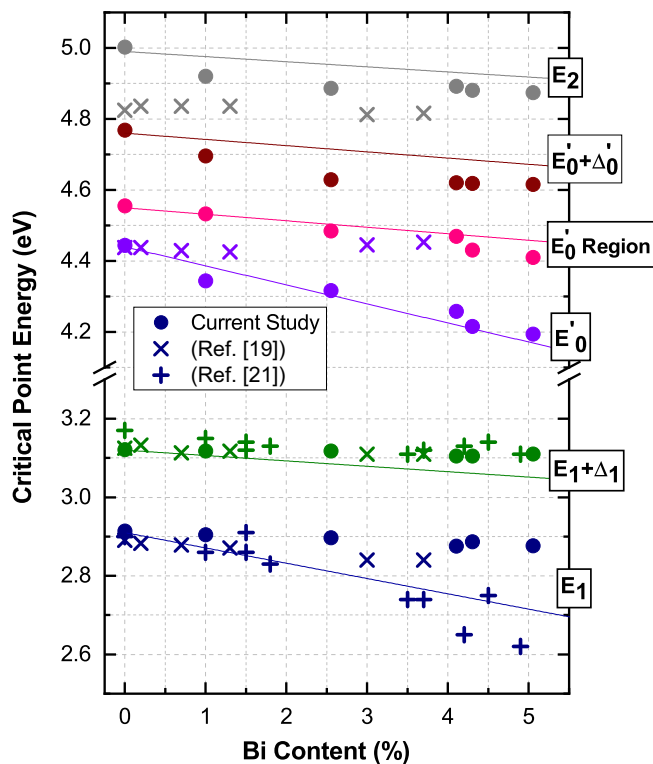
FIG. 14. Comparison of the Bi concentration dependence of the energy of the critical points measured by Ben Sedrine *et al.* ($\times$) [19] and Bushell *et al.* (+) [21] with the results of this paper (•) along with the fitted lines from Fig. 11.
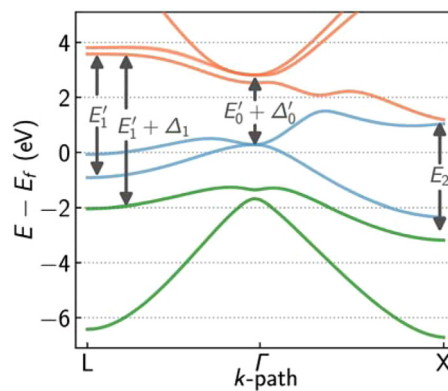


FIG. 15. DFT calculations of the GaBi band structure identifying the critical points in Table I. The bands in green, blue, and orange represent occupied, partially occupied, and unoccupied bands, respectively.

an expanded band splitting is present in the valence bands of GaBi when compared to the GaAs band structure, so that the $E_2$ critical point can be expected to separate into several critical points in GaBi. The energy range for these critical points is shown in Table I. In the case of the experimentally rather broad $E_1'$ critical point, the spin-orbit splitting in GaAs is not resolved; the splitting is much larger for GaBi; therefore we include the energies for both $E_1'$ and $E_1' + \Delta_1$ in Table I.

## V. CONCLUSIONS

Using spectroscopic ellipsometry in the energy range from 0.37 to 9 eV we have measured 11 different critical points in the complex dielectric function for 11 different $GaAs_{1-x}Bi_x$ epitaxial thin films with Bi concentrations ranging from 1% to 17%. The ellipsometry results are in good agreement with other measurements of the optical band gap and the split-off hole band gap. Most of the critical points extrapolate back to GaAs critical points at a Bi concentration of 0%. Our measurements show that the top of the valence band is the part of the band structure that is most strongly dependent on Bi content. By comparison, other parts of the band structure are relatively insensitive to Bi alloying. In addition, an interesting critical point is observed that we attribute to alternative allowed optical transitions made possible by changes to the top of the valence band in the Bi alloy caused by resonant interactions with Bi orbitals. Several of the critical points can be extrapolated to 100% Bi where they show reasonable agreement with the calculated band structure of GaBi. We find that the refractive index of GaAs in the near-infrared region

These results are consistent with the result in Ref. [6] that the band gap of GaBi is $-1.45$ eV. We do not attempt to compare the extrapolated measurements for these critical points with the calculated band structure for GaBi. Also the Bi concentration dependence of the band gap $E_0$ shows significant bowing as discussed above. Without reliable information on the composition dependence of the bowing parameter an extrapolation of $E_0$ to 100% Bi is not convincing. The values for the $E_1 + \Delta_1, E_0' + \Delta_0', E_2, E_1'$ critical points extrapolated to 100% Bi are listed in Table I together with DFT calculation as shown in Fig. 15 and other theoretical values from the band structure calculations of GaBi [6,53].

The extrapolated values are in reasonable agreement with the band structure of Janotti *et al.* [6] and Ferhat and Zaoui [53] as shown in Table I. We have not attempted to compare the extrapolated critical points for GaBi with the other band structure calulations [50,51,54,55] because these calculations do not include spin-orbit coupling. In the case of the $X$ point,

TABLE I. Critical points for GaAs and GaBi in eV.

| CP | GaAs [22,26] | GaAs (ellipsometry) | GaBi (ellipsometry, extrapolated) | GaBi (DFT) | GaBi [6] | GaBi [53] |
|---|---|---|---|---|---|---|
| $E_1 + \Delta_1$ | 3.2 | 3.1 | 1.9 | 1.96 | 2.0 | 2.1 |
| $E_0' + \Delta_0'$ | 4.7 | 4.7 | 3.1 | 2.53 | 2.3 | 2.4 |
| $E_2$ | 5.0 | 5.0 | 3.6 | 3.40–4.36 | 3.5–4.6 | 3.0–4.0 |
| $E_1', E_1' + \Delta_1$ | 6.5, 6.8 | 6.5 | 5.5 | 4.50, 5.61 | 4.6, 5.5 | 3.2, 5.8 |

near the band gap is $6\times$ more sensitive to bismuth content than it is to indium content.

[1] Z. Batool *et al.*, in *Molecular Beam Epitaxy: From Research to Production*, edited by M. Henini (Elsevier, Amsterdam, 2013), Chap. 7, p. 139.

[2] X. Lu, D. A. Beaton, R. B. Lewis, T. Tiedje, and Y. Zhang, Appl. Phys. Lett. **95**, 041903 (2009).

[3] S. Francoeur, M. J. Seong, A. Mascarenhas, S. Tixier, M. Adamcyk, and T. Tiedje, Appl. Phys. Lett. **82**, 3874 (2003).

[4] G. Leibiger, V. Gottschalch, V. Riede, M. Schubert, J. N. Hilfiker, and T. E. Tiwald, Phys. Rev. B **67**, 195205 (2003).

[5] G. Leibiger, V. Gottschalch, M. Schubert, G. Benndorf, and R. Schwabe, Phys. Rev. B **65**, 245207 (2002).

[6] A. Janotti, S. H. Wei, and S. B. Zhang, Phys. Rev. B **65**, 115203 (2002).

[7] S. Tixier, M. Adamcyk, T. Tiedje, S. Francoeur, A. Mascarenhas, P. Wei, and F. Schiettekatte, Appl. Phys. Lett. **82**, 2245 (2003).

[8] P. Wang, W. Pan, X. Wu, C. Cao, S. Wang, and Q. Gong, Appl. Phys. Express **9**, 045502 (2016).

[9] V. Bahrami-Yekta, Optimization of growth conditions of GaAs$_{1-x}$Bi$_x$ Alloys for laser applications, Doctoral dissertation, University of Victoria, 2015.

[10] V. Bahrami-Yekta, T. Tiedje, and M. Masnadi-Shirazi, Semicond. Sci. Technol. **30**, 094007 (2015).

[11] T. M. Christian, K. Alberi, D. A. Beaton, B. Fluegel, and A. Mascarenhas, Jpn. J. Appl. Phys. **56**, 035801 (2017).

[12] C. Z. Zhao, H. Y Ren, T. Wei, S. S. Wang, and K. Q. Lu, J. Electron. Mater. **47**, 4539 (2018).

[13] S. Zollner, J. Appl. Phys. **90**, 515 (2001).

[14] D. E. Aspnes and A. A. Studna, Phys. Rev. B **27**, 985 (1983).

[15] J. A. Woollam, B. Johs, C. M. Herzinger, J. Hilfiker, R. Synowicki, and C. L. Bungay, Proc. SPIE **CR72**, 3 (2000).

[16] B. Johs, J. A. Woollam, C. M. Herzinger, J. Hilfiker, R. Synowicki, and C. L. Bungay, Proc. SPIE **CR72**, 29 (2000).

[17] *Handbook of Ellipsometry*, edited by H. G. Tompkins and E. A. Irene (William Andrew Publishing, Norwich, NY, 2005).

[18] H. Fujiwara, *Spectroscopic Ellipsometry, Principles and Applications* (John Wiley & Sons, New York, 2007).

[19] N. Ben Sedrine, I. Moussa, H. Fitouri, A. Rebey, B. E. Jani, and R. Chtourou, Appl. Phys. Lett. **95**, 011910 (2009).

[20] S. Tumėnas, V. Karpus, K. Bertulis, and H. Arwin, Phys. Status Solidi C **9**, 1633 (2012).

[21] Z. L. Bushell, R. M. Joseph, L. Nattermann, P. Ludewig, K. Volz, J. L. Keddie, and S. J. Sweeney, J. Appl. Phys. **123**, 045701 (2018).

[22] P. Lautenschlager, M. Garriga, S. Logothetidis, and M. Cardona, Phys. Rev. B **35**, 9174 (1987).

[23] S. R. Johnson, C. Lavoie, T. Tiedje, and J. A. Mackenzie, J. Vac. Sci. Technol. B **11**, 1007 (1993).

[24] *Handbook of Optical Constants of Solids*, edited by E. D. Palik (Elsevier, Amsterdam, 1997), Vol. 1, pp. 429–443.

[25] S. Zollner, Appl. Phys. Lett. **63**, 2523 (1993).

[26] J. R. Chelikowsky and M. L. Cohen, Phys. Rev. B **14**, 556 (1976).

[27] C. C. Kim, J. W. Garland, H. Abad, and P. M. Raccah, Phys. Rev. B **45**, 11749 (1992).

[28] D. E. Aspnes, in *Handbook on Semiconductors*, Vol. 2, edited by M. Balkanski (North-Holland, Amsterdam, 1980), Chap. 4A.

[29] A. Savitzky and J. E. Golay, Anal. Chem. **36**, 1627 (1964).

[30] J. Steinier, Y. Termonia, and J. Deltour, Anal. Chem. **44**, 1906 (1972).

[31] P. E. Blöchl, Phys. Rev. B **50**, 17953 (1994).

[32] G. Kresse and D. Joubert, Phys. Rev. B **59**, 1758 (1999).

[33] G. Kresse and J. Hafner, Phys. Rev. B **47**, 558 (1993); **49**, 14251 (1994).

[34] G. Kresse and J. Furthmüller, Comput. Mater. Sci. **6**, 15 (1996); Phys. Rev. B **54**, 11169 (1996).

[35] A. Zunger, S.-H. Wei, L. G. Ferreira, and J. E. Bernard, Phys. Rev. Lett. **65**, 353 (1990).

[36] S.-H. Wei, L. G. Ferreira, J. E. Bernard, and A. Zunger, Phys. Rev. B **42**, 9622 (1990).

[37] A. van de Walle, M. Asta, and G. Ceder, CALPHAD: Comput. Coupling Phase Diagrams Thermochem. **26**, 539 (2002).

[38] A. van de Walle, CALPHAD: Comput. Coupling Phase Diagrams Thermochem. **33**, 266 (2009).

[39] A. van de Walle, P. Tiwary, M. de Jong, D. L. Olmsted, M. Asta, A. Dick, D. Shin, Y. Wang, L. Q. Chen, and Z. K. Liu, CALPHAD: Comput. Coupling Phase Diagrams Thermochem. **42**, 13 (2013).

[40] J. P. Perdew, A. Ruzsinszky, G. I. Csonka, O. A. Vydrov, G. E. Scuseria, L. A. Constantin, X. Zhou, and K. Burke, Phys. Rev. Lett. **100**, 136406 (2008).

[41] F. Tran and P. Blaha, Phys. Rev. Lett. **102**, 226401 (2009).

[42] L. C. Bannow, S. C. Badescu, J. Hader, J. V. Moloney, and S. W. Koch, Appl. Phys. Lett. **111**, 182103 (2017).

[43] P. V. C. Medeiros, S. Stafström, and J. Björk, Phys. Rev. B **89**, 041407(R) (2014).

[44] P. V. C. Medeiros, S. S. Tsirkin, S. Stafström, and J. Björk, Phys. Rev. B **91**, 041116(R) (2015).

[45] B. Fluegel, S. Francoeur, A. Mascarenhas, S. Tixier, E. C. Young, and T. Tiedje, Phys. Rev. Lett. **97**, 067205 (2006).

[46] M. Masnadi-Shirazi, R. B. Lewis, V. Bahrami-Yekta, T. Tiedje, M. Chicoine, and P. Servati, J. Appl. Phys. **116**, 223506 (2014).

[47] A. G. Thompson and J. C. Woolley, Can. J. Phys. **45**, 255 (1967).

[48] C. P. Kuo, S. K. Vong, R. M. Cohen, and G. B. Stringfellow, J. Appl. Phys. **57**, 5428 (1985).

[49] I. Vurgaftman, J. R. Meyer, and L. R. Ram-Mohan, J. Appl. Phys. **89**, 5815 (2001).

[50] S. Zollner, M. Garriga, J. Kircher, J. Humlicek, M. Cardona, and G. Neuhold, Phys. Rev. B **48**, 7915 (1993).

[51] A. Abdiche, H. Abid, R. Riane, and A. Bouaza, Phys. B (Amsterdam, Neth.) **405**, 2311 (2010).

[52] N. A. A. Rahim, R. Ahmed, B. Ul Haq, M. Mohamad, A. Shaari, N. Ali, and S. Goumri-Said, Comput. Mater. Sci. **114**, 40 (2016).

[53] M. Ferhat and A. Zaoui, Phys. Rev. B **73**, 115107 (2006).

[54] H. Achour, S. Louhibi, B. Amrani, A. Tebboune, and N. Sekkel, Superlattices Microstruct. **44**, 223 (2008).

[55] A. H. Reshak, H. Kamarudin, S. Auluck, and I. V. Kityk, J. Solid State Chem. **186**, 47 (2012).

[56] Yu. A. Goldberg and N. M. Schmidt, in *Handbook Series on Semiconductor Parameters*, edited by M. Levinshtein, S. Rumyantsev, and M. Shur (World Scientific, London, 1999) Vol. 2, pp. 62–88.